Thermospectroscopic infrared imaging of a confined drying process

M. Lehtihet, E. Abisset, S. Chevalier, Alain Sommier, Christophe Pradere, J. Leng

Thermospectroscopic Infrared Imaging of a Confined Drying Process

M. Lehtihet[a,b,*], E. Abisset[b], S. Chevalier[b], A. Sommier[b], C. Pradere[b], J. Leng[a]

[a] *Univ. Bordeaux, Laboratory of the Future, CNRS/Solvay, 178 avenue du Docteur Albert Schweitzer, F-33608 Pessac, France*
[b] *I2M, UMR CNRS-ENSAM no 5295, Esplanade des Arts et Metiers, F-33405 Talence, France*

Abstract

We present an infrared (IR) imaging technique that allows us to retrieve quantitative concentration and thermal maps with relatively fast acquisition times for samples that are evolving in time and have micron-scale spatial resolution. As a proof-of-concept, we image the transient drying kinetics of a μL drop of colloidal suspension in a confined geometry. Quantitative concentration maps inside the drying droplet are retrieved. Transport phenomena such as colloid redistribution inside the droplet due to inhomogeneous drying can be highlighted by this means. A numerical inverse method based on the acquired images that allows one to estimate intrinsic properties of the studied material, such as the collective diffusion coefficient of the mixture, is presented. Such a technique combined with statistical inverse methods provides a useful, non-invasive means of visualizing and estimating parameters of materials evolving in time.

Keywords: Thermospectroscopy, Infrared imaging, Silica dispersion, Confined drying, Transport properties

1. Introduction

Regarding transient systems, such as the drying of a material, the transient measurement of concentration fields is of interest to industries concerned with non-destructive control problems. However, it still remains a challenge. Most techniques used for local composition estimation require long acquisition times and do not allow imaging of the system under study, as in Raman spectrometry [1]. Among the dispersive spectroscopy techniques (in contrast to interferometric spectroscopy techniques such as Fourier transform infrared spectroscopy [2]), very few afford the possibility of obtaining quantitative composition maps alongside temperature everywhere in the sample in a small duration. Indeed, various industrial methods for material fabrication rely, among other methods, on the use of a drying process, which introduces many heat and mass transfers occurring on short scales of a few μm and short time scales, making their imaging a difficult task. The authors in [3] developed novel instrumentation and processing to perform simultaneous micro-scale thermography and spectroscopy in the infrared range and applied it to reveal the temperature-induced phase change occurring in paraffin wax n-alkane. The authors particularly emphasize how this versatile and flexible technique is well adapted to characterize many systems in which the mass and heat transfer effects are coupled. With the implementation of automated acquisition of this technique, the kinetics of the concentration and temperature fields can be visualized, making it a suitable probing method for drying processes (among other transient systems where these two transport mechanisms are prone to occur). This technique is tested on a model transient system, the confined drying of a drop of colloidal dispersion, as it is a well-known problem on which theoretical models have been tested and validated in the literature [4, 5]. The authors in reference [6] studied such a confined drying process of a Ludox silica nanoparticle dispersion using Raman spectroscopy and highlighted the concentration gradients of colloids that appear over time. However, concentration fields may only be accessed along a diameter of the drop using Raman spectroscopy as no imaging is possible. Furthermore, no coupling with temperature of the studied sample is possible due to the wavelength of operation of Raman spectroscopy. Yet, real-time acquisition of thermal and spectroscopic images is interest for a complete characterization of samples and could be successfully combined with inverse methods for estimation of intrinsic properties of the material itself.

We propose here a multispectral imaging technique allowing the estimation of transient 2D concentration fields with a fast acquisition time. We apply it to the same model drying process as in [6] and demonstrate the ability of our IR imaging technique to retrieve concentration fields and shape simultaneously, with relatively good accuracy. Spectroscopic and thermal hypercubes of data are acquired as the drying goes on and a careful autocalibration procedure based on the

*Corresponding author
Email addresses: mohamedmoncef.lehtihet-ext@solvay.com (M. Lehtihet), emmanuelle.abisset-chavanne@ensam.eu (E. Abisset), stephane.chevalier@u-bordeaux.fr (S. Chevalier), alain.sommier@u-bordeaux.fr (A. Sommier), christophe.pradere@u-bordeaux.fr (C. Pradere), jacques.leng-exterieur@solvay.com (J. Leng)

absorbance raw images is presented for the retrieval of local chemical composition at each pixel of the images. We also use a statistical method based on the acquired images to estimate intrinsic properties of the material under study, such as its diffusivity in its host solvent. Maps of the collective diffusion coefficient of a silica/water mixture inside the droplet are retrieved by this means.

2. Thermospectroscopy IR imaging technique

As depicted in Figure 1, a thermospectroscopy setup operating in the IR range is used to observe the confined drying of a colloidal dispersion of silica nanoparticles, both in transmission and emission mode [3]. This technique allows us to acquire both the thermal emission and transmitted intensity simultaneously, from which both temperature and concentration fields can be retrieved at relatively high acquisition rates up to 500 Hz. An IR source emitting blackbody radiation is coupled to a monochromator with diffraction gratings allowing one to select wavelengths between $\lambda = 400$ nm and $\lambda = 20$ μm. Detection is realized by a FLIR InSb camera collecting the signal with its proper sensitivity comprised between $\lambda = 1.9$ μm and $\lambda = 5.5$ μm. Microscope lenses are used to focus the IR beam on the studied sample with a resolution of 20×20 μm^2. Furthermore, 110 wavelengths can be acquired with an acquisition time of approximately 15 seconds. Hence, a transient system can be imaged at several wavelengths with a given acquisition frequency of the camera. The thermal emission and transmitted intensity will be superimposed at the output of the sample and to dissociate them afterward, a splitter (chopper) placed inside the monochromator is used to either block or transmit the monochromatic beam. An adequate synchronization of the camera with this splitter allows one to acquire two signals: the thermal emission alone when the splitter blocks the incident light and the sum of the thermal emission and transmitted light when the splitter is open. These two signals are then numerically dissociated after the acquisition is done. This technique then allows us to obtain hypercubes of raw data in x, y, λ and t for these two signals. To measure high attenuation coefficients typical of water in the near-infrared range, high integration times of the IR camera are necessary. However, they introduce the problem of measuring the unhindered beam at the same integration time as the one used for the sample. The unhindered beam at such a high integration time often saturates the detector array of the camera, making the calculation of transmittance images impossible. To overcome this technical limitation, the calibration procedure presented in [7] is used, which consists in making several acquisitions over the studied spectral range for different integration times of the camera and extrapolating a "numerical unhindered beam" at high integration times for which the camera would be normally saturated. This procedure allows one to bypass the saturation limits of the IR camera and estimate attenuation coefficients in highly absorbing compounds.

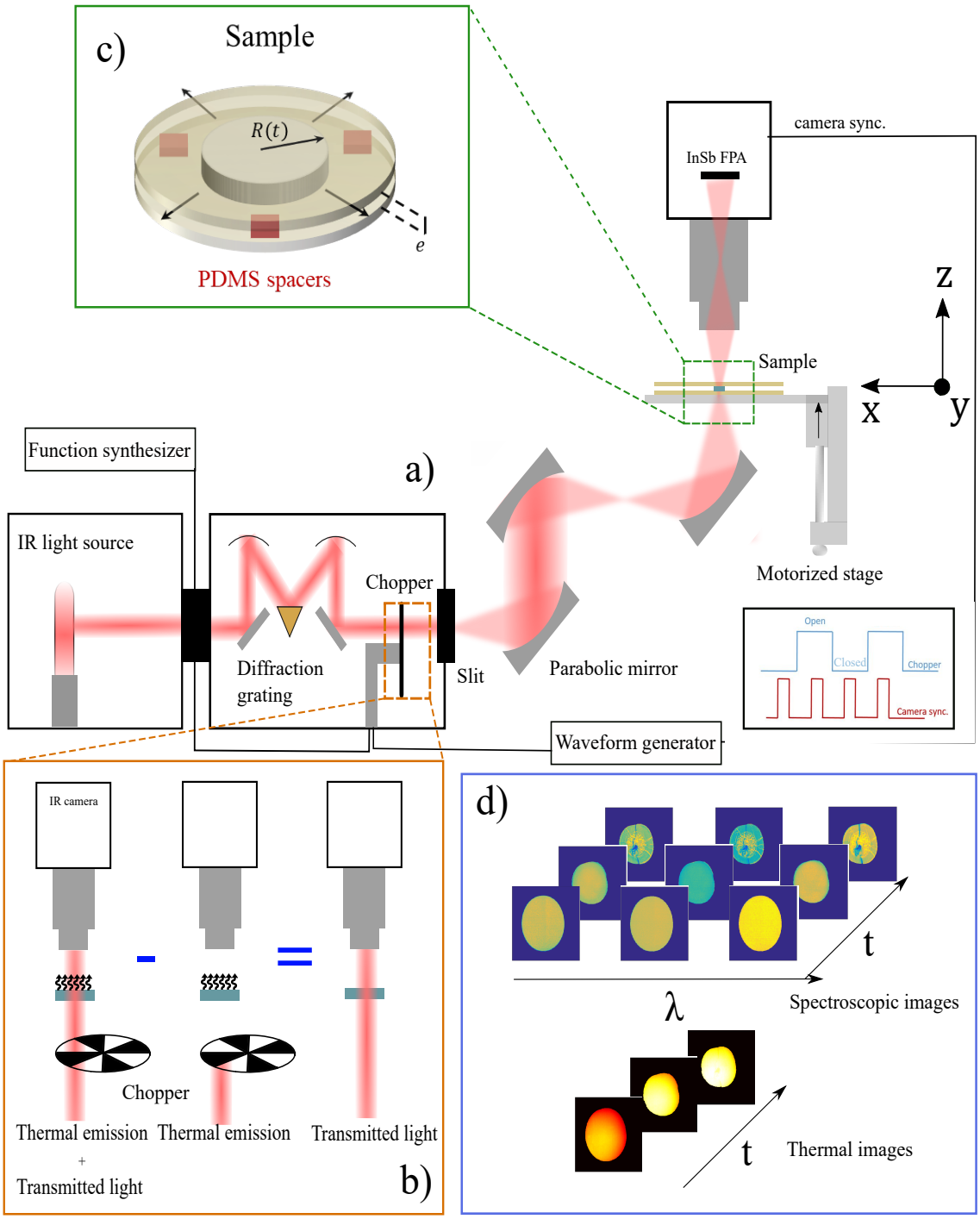

Figure 1: a) Schematic of the thermospectroscopy setup used in the present study, composed of an IR light source coupled to a diffraction grating to produce a monochromatic beam, a set of mirrors used to illuminate the studied sample and an InSb focal plane array (FPA) camera to collect the transmitted light. b) Scheme of the signal numerical separation. Using the synchronization between the camera and the splitter, the simultaneous acquisition of both the thermal emission E (in black curved lines) and the transmitted light T (in red) of the confined drop can be achieved and hypercubes of E and T are acquired c) Schematic of the cell containing the dispersion droplet (not in scale), with a confinement fixed by PDMS spacers. d) Example of acquired spectroscopic and thermal images acquired using the present setup. Transient systems can be imaged with good spatial and temporal resolution.

3. IR imaging of confined drying of colloidal dispersion

3.1. Imaging the drying process: raw images

Using the setup presented in the previous section, we realize the imaging of a colloidal dispersion drop of Ludox AS40 (Sigma-Aldrich) silica nanoparticles (r = 11 nm, initial volume fraction $\varphi_0 = 0.24$) confined between two 370-μm thick silicon (Si) wafers with spacers of 50 μm in thickness. The wafers are surface treated with a thin layer of poly(dimethylsiloxane) (PDMS) of approximately 20 μm in thickness deposited by spin-coating to make them hydrophobic and make sure that the drying of the droplet occurs without pinning of the meniscus on the substrate. In such a configuration, drying occurs along the perimeter of the drop and is therefore governed mainly by a diffusive mass transfer of water vapour from the edge of the drop to the edge of the cell. Regularly during the drying, thermal and spectroscopic images are acquired as films of the ongoing drying process, with a lateral resolution of approximately 20 μm per pixel. We are therefore able to represent absorbance and thermal emission everywhere inside the droplet and at any time (figures 2 and 3) and highlight the distribution of water during drying (which is highly absorbing in the mid-infrared range). The system undergoes a continuous transition from liquid dispersion to an amorphous packing of silica nanoparticles through which water dries until the porous structure eventually breaks and delaminates [8]. The system becomes heterogeneous after the breaking, as seen on the absorbance images at the last instants.

Thermal images are acquired in Digital Level units, which are intensity units proper to IR cameras. A subtle decrease in thermal emission is observed at the edge. However, a 2D analytical model of the confined water drop between two Si/PDMS substrates suggests that the drop remains isothermal, with a very low cooling effect at the edge due to endothermic vapourization ($\Delta T_{\text{edge}} \approx -0.014$°C); this model calculates the equilibrium temperature of the drop through the energy balance between vapourization at the edge and the thermal conduction at the liquid/substrate interface as detailed in the Supplementary Material. In Figure 3, the emissive variations may arise from the dependency of the emissivity of the mixture with its local composition, an issue which is not addressed here. Instead, we focus our attention on the spectroscopic images on which numerical methods will work to obtain the concentration of colloids and collective diffusion coefficient everywhere inside the sample.

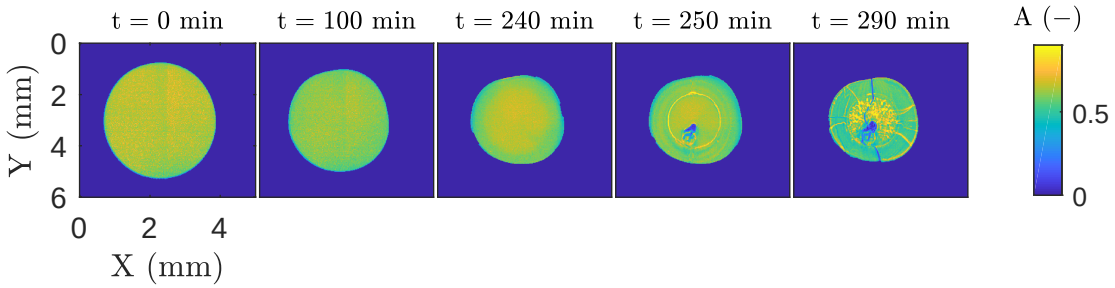

Figure 2: Mapping of IR absorbance ($\lambda = 4.5$ μm) of the silica dispersion droplet as function of time.

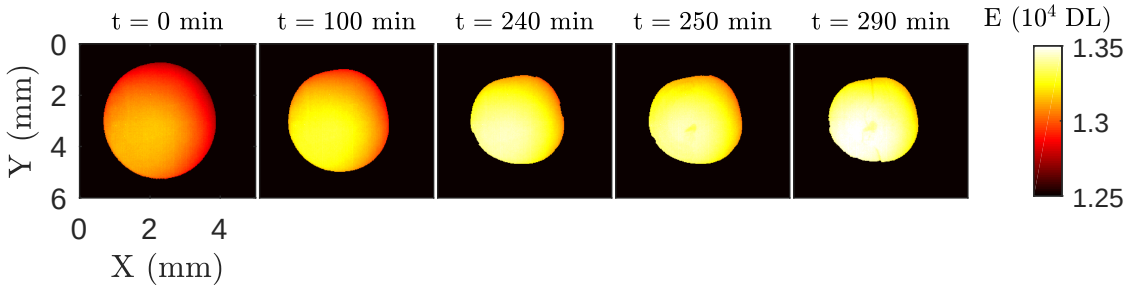

Figure 3: Proper emission of the drop in Digital Levels (DL) acquired by the IR camera as function of time.

3.2. Drying kinetics

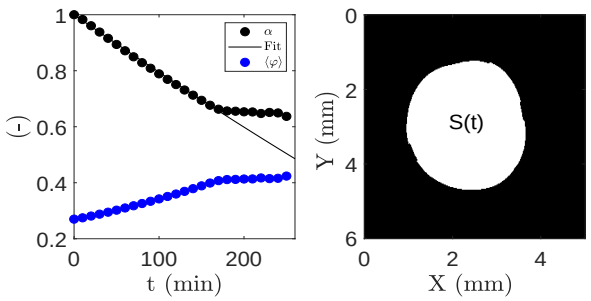

Figure 4: Evolution of normalized area with respect to the initial area, with time in black dots against the drying equation analytical solution for the fitted value of the vapour diffusivity in the solid black line. Estimated mean volume fraction of colloids inside the drop in blue dots

The drying kinetics of the confined drop have been intensively studied in the literature [5, 6, 9, 10] and modelled for pure solvent drops and dispersions. In the case of the pure solvent drop squeezed between two substrates, evaporation proceeds by gas diffusion from the meniscus of the drop, where the atmosphere is assumed to be saturated in vapour, towards the edge of the cell where the atmosphere is at some relative humidity. For small cell spacers (a few tens of μm), the drop can be assumed to be two-dimensional, and the receding of the meniscus is governed by flux conservation at this position, which reads [9]:

$$\ln(\alpha\beta)\frac{\mathrm{d}\alpha\beta}{\mathrm{d}t} = \frac{1}{\tau_e}, \tag{1}$$

with the following reduced variables: $\alpha(t) = S(t)/S(0)$ is the area of the droplet $S(t)$ (m^2) normalized by its initial value $S(0)$, $\beta = S(0)/S_w$ the ratio between the initial drop area and the area of the wafers and $\tau_e = S_w/4\pi\tilde{D}$ (s) a characteristic time of evaporation (i.e., the drying time of a drop of pure water with the same initial radius and evaporating in the same conditions); $\tilde{D}$ (m^2.s^{-1}) represents the diffusion coefficient of the water vapour in air D_{vap} reduced to account for the density balance between the liquid and the gas [5]. This equation expresses the effect of confining a drop on its drying kinetics. Indeed, the finite size of the wafers imposes a distance in which the water vapour coming from the drop must escape; therefore, the radius R_w of the wafers is of paramount importance for tuning the evaporation of the drop. The Si wafers used here have a radius $R_w = 3.65$ cm, inducing drying with a duration of approximately a few hours. An analytical solution of the drying equation is as follows:

$$t = \tau_e[\alpha\beta\ (\ln(\alpha\beta) - 1) - \beta\ (\ln(\beta) - 1)]. \tag{2}$$

Therefore, by using image segmentation on our images to estimate α at any instant, we may estimate the water vapour diffusivity D_{vap} using the theoretical model 2. The agreement between measurements and this model is shown in 4, for a fitting value of $D_{\mathrm{vap}} \approx 2.9\,10^{-5}$ m^2.s^{-1} which is in good agreement with tabulated values [11]. We observe that after a certain time, the area of the drop no longer evolves, and hence deviates significantly from the values predicted by the evaporation model as the latter holds for pure solvents only, not for dispersions.

Due to the (PDMS) treatment on the Si wafers, the drop can move without pinning on the substrate, inducing no silica deposit on the wafers and allowing us to consider that the silica volume is conserved inside the drop at any time as expressed by [you were talking about mass and wrote an equation about volume] $\langle\varphi(t)\rangle S(t) = \varphi_0 S(0)$ assuming constant thickness of the drop, or equivalently:

$$\langle\varphi(t)\rangle = \frac{1}{S(t)}\int_0^{R(t)} \varphi(r)2\pi r\mathrm{d}r = \varphi_0\frac{S(0)}{S(t)} = \frac{\varphi_0}{\alpha}, \tag{3}$$

where $\varphi(t)$ is the volume fraction of silica in the dispersion and $\varphi_0 \equiv \varphi(t=0)$ its initial value. The calculation of $\varphi(t)$ is shown in Figure 4.

The thermospectrometry imaging technique presented above leads to both the concentration and the shape of the drop simultaneously, which contrasts with other techniques such as Raman spectroscopy [6] or optical microscopy [5] which provide either the concentration field or the shape respectively. This simultaneous acquisition allows us to establish a calibration procedure between the mean absorbance of the drop and the estimated mean volume fraction to retrieve colloid concentration fields.

3.3. Calibration procedure

To obtain concentration fields within the drop, we present a calibration procedure which permits us to bypass some instrumental difficulties: indeed, absorbance images measured by any classic spectrometer do not illustrate *the absorbance of the studied sample* but are prone to be altered by many instrumental artefacts (imperfect monochromatic incident beam, transfer function of the monochromator, quantum efficiency of the array of detectors, etc.) and effects due to the cell and the material itself (light scattering by the nanoparticles, refractive index contrast between empty and full cell, etc.). As the silica nanoparticles have a very small diameter compared to the incident wavelength, scattering is negligible compared to water absorption, but our data may nevertheless be affected by instrumental and cell biasses. Retrieving true absorbance images is thus a difficult task as one would need, for example, to completely calculate the Fresnel reflectance coefficients at all the interfaces of the cell and cancel their effects on the acquired images or measure the transfer function of the instrument in parallel. Directly converting the images into concentration fields is therefore of interest as it allows us to bypass this instrumental bias.

To do so, we use a self-consistent method already performed in [6] and quoted as the 'auto-calibration method', relying on the assumption that no colloids are left over on the substrates during drying (i.e., volume conservation of silica within the drop, Eq. (3)). We take advantage of the imaging ability of the setup (absorbance images) to affect to the average absorbance $\langle A \rangle$ the average volume fraction φ/α. To complete the dataset, we place drops of the original silica dispersion, the same dispersion diluted two times, and a drop of pure water and measure the mean absorbance immediately after confining (i.e., no drying has occured). Beside, the mass fraction of the dispersion are separately measured by a dry extract. This dataset is shown in Figure 5 and clearly evidences an affine relationship between $\langle \varphi \rangle$ and $\langle A \rangle$:

$$\langle A \rangle = p_1(\lambda)\langle \varphi \rangle + p_2(\lambda), \tag{4}$$

where the two coefficients $p_1(\lambda)$ and $p_2(\lambda)$ are estimated from the fit at all wavelengths but shown in Fig. 5 for three wavelengths only for clarity reasons.

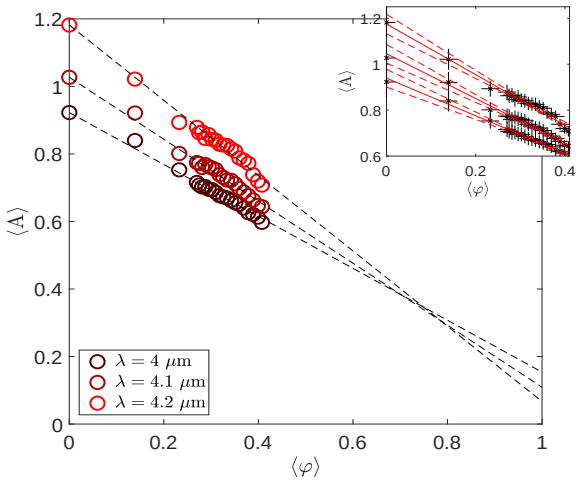

Figure 5: Calibration curves shown here for 3 wavelengths (out of one hundred). (Inset) Experimental data with error bars shown with the linear fit curve in solid line and (95%) confidence bounds in dashed lines.

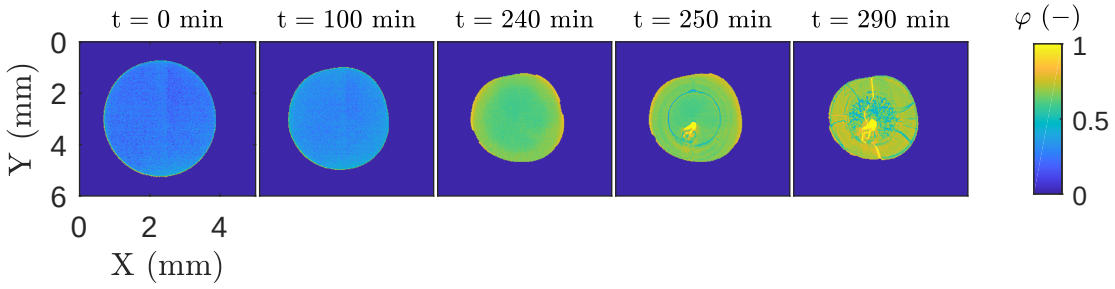

Figure 6: Volume fraction of colloids inside the drop estimated by the calibration procedure. Whenever $\varphi > 0.4$, the concentration should be taken with care as is stands out of the the calibration range validity.

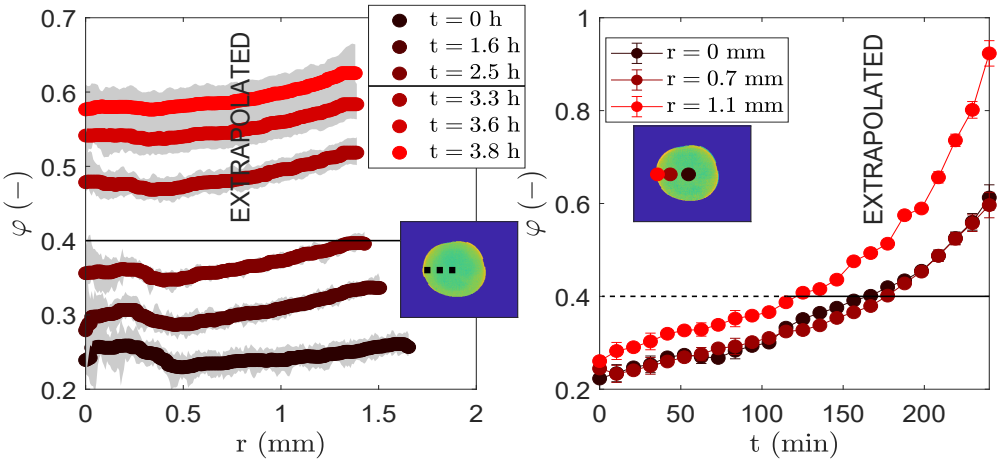

Figure 7: (Left) Colloid volume fraction with respect to position along a radius of the drop averaged over all wavelengths acquired with the standard deviation as confidence intervals in grey. The colour evolution from black to red indicates the increasing time. We observe the establishment of concentration gradients from the centre to the edge of the drop. After 220 min, the silica gel breaks, and the concentration profile is not shown for these times. (Right) Volume fraction shown for three different pixels with respect to time. Notice that the calibration procedure is limited to $\varphi \approx 0.4$, see Fig. 5. Above this volume fraction value, data are extrapolated from the fit yet they are out of the validity range of the calibration procedure; they are shown for the sake of illustration but are not used for further analysis.

The images of Figure 6 show an increase of the volume fraction of colloids with time consistent with a drying kinetics. The image at the last instant shows the heterogeneous material obtained at the end of a confined drying, as we can observe water pockets in the centre of the drop surrounding the hole that has formed during drying (likely due to a trapped air bubble or by the mechanical constraints highlighted by the authors in [12]). By representing the colloid volume fraction along a radius of the drop for several instants, we can highlight the concentration gradients extending from the centre to the edge of the drop. These gradients are the signature of the concentration heterogeneities induced by drying. Such an observation was already made in [6] on the same system, and we obtain an identical result using the present imaging technique with, in addition, a full picture of the concentration field.

4. Estimation of mass diffusivity

4.1. Estimation from boundary condition

The concentration maps (Fig. 6) and profiles (Fig. 7, right) reveal smooth gradients with no crust at the edge of the drop [8] and following Loussert and co. [6], we fit the profiles with a parabolas:

$$\varphi(r,t) = \varphi_c(t)\left[1+\gamma\left(\frac{r}{R}\right)^2\right], \tag{5}$$

where $\varphi_c(t)$ is the colloid volume fraction at $r = 0$. We monitor here that gradients are weak with $\gamma \ll 1$.

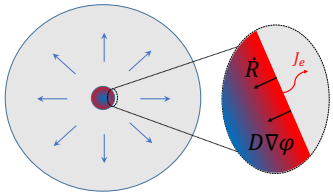

Figure 8: Top schematic view of a confined drop undergoing drying. The colour gradient represents the concentration gradients of colloids from the centre to the edge of the drop: the evaporation flux j_e drives the receding of the meniscus at a velocity $\dot{R}$ which in turn generates concentration gradients of colloids inside the drop and subsequent mass diffusion $D\nabla(\varphi)$ that depends on the collective diffusion coefficient $D \equiv D(\varphi)$ of the dispersion.

It is demonstrated in the Supplementary Material that the drop remains essentially isothermal during the drying kinetics and there is thus no coupling between heat and mass transfers. Furthermore, even though concentration gradients in confined geometries are prone to induce buoyancy-driven flows [13], such convective movement becomes vanishingly small as compared to diffusion for small thickness (say $< 100\,\mu$m, a regime of moderate Rayleigh number Ra, [14]). Therefore, we assume that the mass transport in such a configuration reduces to a competition between evaporation and diffusion mechanism which translates into a boundary condition, see Figure. 8, expressing this balance:

$$-[D(\varphi)\nabla\varphi]_{r=R} = \varphi(R)\dot{R}, \tag{6}$$

where D ($\mathrm{m}^2.\mathrm{s}^{-1}$) is the collective diffusion coefficient

of the dispersion. We are therefore able to estimate $D(\varphi)$ from our measurements, as the receding speed $\dot{R}$ is obtained from image segmentation and concentration profiles extracted from our autocalibration procedure. However, to avoid high variation of D induced by derivation of the obtained concentration field, the profiles are fitted with Eq. (5) and $\nabla\varphi(r = R)$ is calculated by direct analytical derivation. Such a procedure is repeated for all wavelengths in our dataset, and the average D is shown in Figure 9. Our result shows reasonable agreement with the results obtained in Ref. [6]. Here, the collective diffusion coefficient first decreases as the average concentration increases followed by a trend change around a value of $\varphi \approx 0.32$. It could be due to a sol/gel transition that the charged silica particles undergo around this concentration [12].

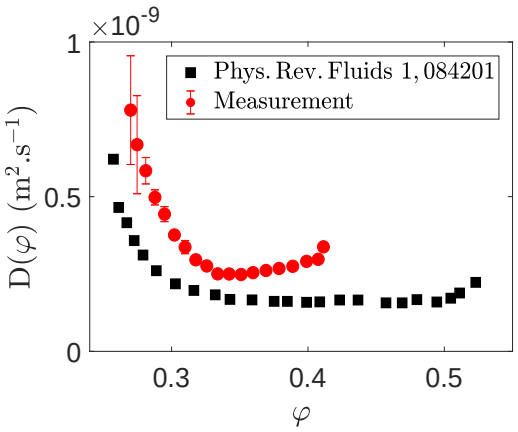

Figure 9: Collective diffusion coefficient of the silica dispersion measured with IR imaging (red disks) and compared with literature data (black squares, [6]).

4.2. Estimation by statistical correlation nodal inverse method

We present now a numerical inverse method developed by Pradere *et al.* [15], Hany *et al.* [16] and Bamford *et al.* [17], where estimations of Péclet fields at steady-state were realized. The method is applied to concentration fields and mass kinetics inside the colloidal drop, as done in the previous work of C. Ravey *et al.* [18]. It consists in evaluating the statistical correlation between time and spatial derivatives of the measured data. This numerical technique is called the *nodal correlation method* as it is an inverse processing method built on a numerical finite difference scheme applied on each node (or pixel of an image).

We start with the usual diffusion equation which we write in a discrete form and where we assume that the discretization is fine enough so that the diffusion coefficient can be considered constant *locally*. The spatial and temporal nodes of the discretization are expressed as r and t respectively and the discrete diffusion equation on the variable φ_{rt} reads:

$$\partial_t \varphi_{rt} = D_{rt} \frac{1}{r} \partial_r (r \partial_r \varphi_{rt}), \tag{7}$$

where $\partial_\alpha \equiv \partial/\partial\alpha$ with $\alpha = r$ or t.

The statistical correlations of the two derivatives are estimated over a fixed time window N_t which represents the number of frames taken for calculations. A correlation coefficient S_{rt} between the Laplacian and temporal derivatives can be calculated, defined as:

$$S_{rt} = \frac{\sum_{t=n}^{n+N_t} \frac{1}{r}\partial_r(r\partial_r\varphi_{rt})\partial_t\varphi_{rt}}{\sqrt{\sum_{t=n}^{n+N_t}\left[\frac{1}{r}\partial_r(r\partial_r\varphi_{rt})\right]^2} \times \sqrt{\sum_{t=n}^{n+N_t}(\partial_t\varphi_{rt})^2}}. \tag{8}$$

This procedure provides a correlation mask S_{rt} that can be applied on the D_{rt} field estimation as a segmentation method *by the physics itself*: it is then possible to estimate the collective diffusion coefficient on each node, especially where the correlation coefficient tends to 1, meaning that the model in Eq. (7) is verified for that position:

$$\frac{1}{D_{rt}} = S_{rt} \frac{\sqrt{\sum_{t=n}^{n+N_t}\left[\frac{1}{r}\partial_r(r\partial_r\varphi_{rt})\right]^2}}{\sqrt{\sum_{t=n}^{n+N_t}(\partial_t\varphi_{rt})^2}} \quad \text{when } S_{rt} \to 1. \tag{9}$$

Notice however that the method suffers from high sensitivity to measurement noise and image post-processing is usually necessary to obtain reliable estimates (e.g., noise filtering method such as singular value decomposition [18]) even though it may introduce a bias. Figure 10 shows images of the absorbance in several sets of coordinates; here, the high signal-to-noise ratio ($S/N \approx 1000$) of the spectroscopic images from the setup should make them suitable for such a numerical method. However, when applying it to the absorbance images for a time window $N_t = 240$ min (corresponding to the time at which the silica gel breaks), the result turns out poorly satisfactory.

We thus propose an alternative method to minimize the noise and which consists in making an integral transform directly on the absorbance A:

$$\Psi(r, \theta, t) = \int_0^r u A(u, \theta, t) \mathrm{d}u, \tag{10}$$

which does not introduce a bias as Ψ remains a physical observable of the problem.

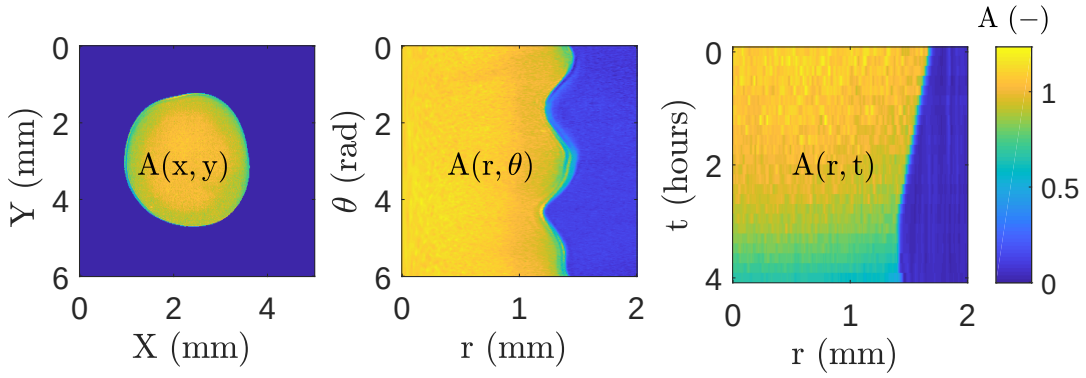

Figure 10: (Left) Raw absorbance image for $\lambda = 4.5$ μm and t = 220 min. (Centre) Transposition of the Cartesian images into polar images. (Right) Space-time image of one radius of the drop as a function of time, showing the receding of the contact line.

With this change of variable, we may rewrite the diffusion equation in an integral form:

$$\partial_t \Psi_{rt} = D_{rt} \left(\partial_{rr} \Psi_{rt} - \frac{1}{r} \partial_r \Psi_{rt} \right) \tag{11}$$

(with ∂_{rr} is the second order spatial derivative) and we study the statistical correlations between the input variables $\partial_t \Psi_{rt}$ and $\left(\partial_{rr} \Psi_{rt} - \frac{1}{r} \partial_r \Psi_{rt}\right)$ in order to evaluate their correlation coefficient and to mask the images through the value of this coefficient. Mapping of the D coefficient can be performed at a certain angle θ for all instants in the fixed time window and repeated over all angles to estimate collective diffusion coefficient maps inside the drop; we expect and checked (not shown) that this quantity does vary significantly with the angle.

The input variables of the inverse method are shown in Figure 11 for a fixed angle in the space-time diagram. The output result of the inverse method is shown in Figure 12 from these input variables and segmentation with the correlation mask. We obtain values of D in the range $2\,10^{-10}$ to $6\,10^{-10}$ m^2.s^{-1}, and we observe an increase of the D coefficient towards the centre of the drop, coherent with the parabolic concentration profiles measured previously. Certain pixels present flaws, as the ones at the first 40 minutes of the drying near the edge of the drop where no estimation occurred. However, the estimated tendency of D at the meniscus position shown in Figure 12 corresponds well to the one obtained by the autocalibration method, with a lighter decrease of D with increasing concentration and low dispersion with θ. For volume fractions below 0.3, some variations of D with θ can be seen, but the trend for all angles is the same after this critical concentration, validating our initial guess of low variation with angle. Finally, we take advantage of the multi-parameter estimation that we possess here and calculate the average D coefficient from all angles weighted by a *temporal weight matrix* $W = \sum_t S_t$, quenching the angle and time parameters:

$$\bar{D}(r) = \frac{\int_\theta W(r,\theta) D(r,\theta)}{\int_\theta W(r,\theta)}. \tag{12}$$

The results are shown in Figure 13 for intervals of two angles where the meniscus speed was different, leading to deformation of the contact line, as seen in the absorbance images in polar coordinates. We observe that the obtained $\bar{D}$ is similar in both cases except near the meniscus position at the first concentration values. This variation may be the signature of various phenomena influencing the transport of colloids (local pinning of the contact line, anisotropic drying, etc.). The collective diffusion coefficient estimation was made as an average over all angles in [6], but our technique allows us to grasp the complicated shapes the drop may adopt and realize estimations under such considerations. It would be of interest to solve diffusion/convection models using this technique to retrieve Peclet fields inside the drop. Furthermore, one may notice that other input variables could be used as a single time and space derivative to estimate velocity fields alongside intrinsic properties as the colloid D coefficient . Finally, the maps of D are obtained after application of the nodal method at every angle of the drop after returning from polar to Cartesian coordinates.

Initially, the water content is high, contributing more noise to the images as water is the most absorbing compound. This is seen on the estimation as the pixels where the estimation did not occur because the correlation threshold is not met (i.e., no sufficiently good enough correlation between the two input variables). As water evaporates, the accuracy of the estimation increases, and we retrieve complete D fields inside the drop. We can observe a collective diffusion coefficient that is higher at the centre of the drop than at the edge, as it depends on the local composition. One may observe that the centre pixel shows no estimated value as it is a singularity in Figure 11, so the nodal method

would not operate. As drying goes on, silica transport inside the drop becomes mainly radial and D maps become invariant by rotation around the centre point. This observation may be explained by the fact that the system goes continuously from a liquid dispersion, in which hydrodynamic phenomena are more likely to occur, to a solid porous material, through which water diffuses following the direction of the vapour phase flux.

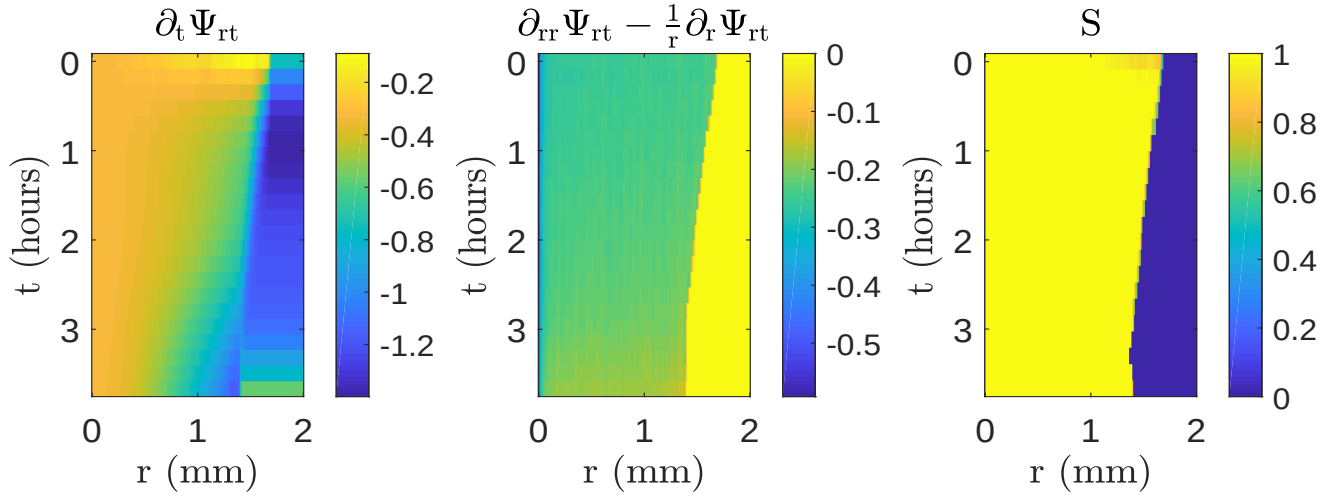

Figure 11: (Left and Centre) Input variables of the inverse method in the space-time diagram for a fixed angle of $\theta = 30°$ (Right) Correlation mask obtained at the same angle

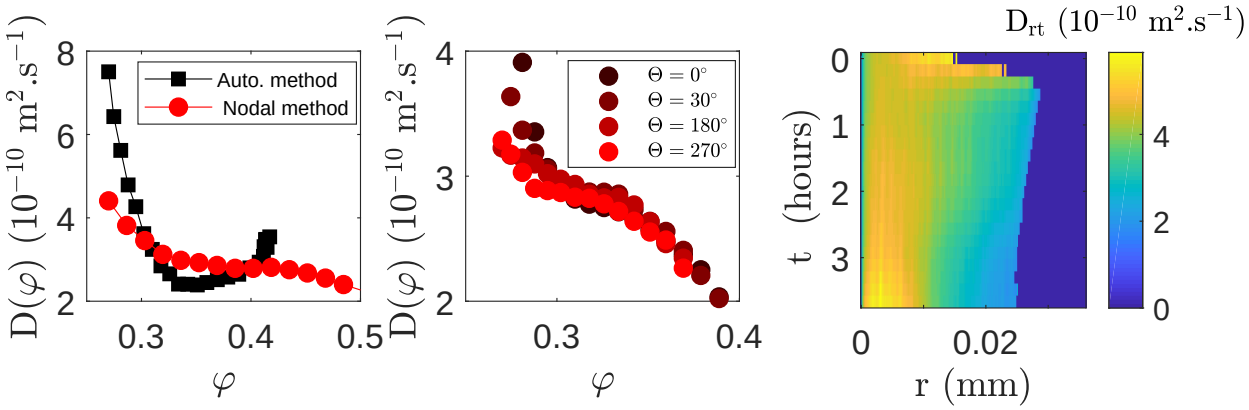

Figure 12: (Left) Collective diffusion coefficient estimated at the meniscus position versus the result from the autocalibration procedure. (Middle) Collective diffusion coefficient at the same position for some angles of the study. (Right) Collective diffusion coefficient of colloids estimated by the inverse method in the space-time diagram for a fixed angle of $\theta = 30°$.

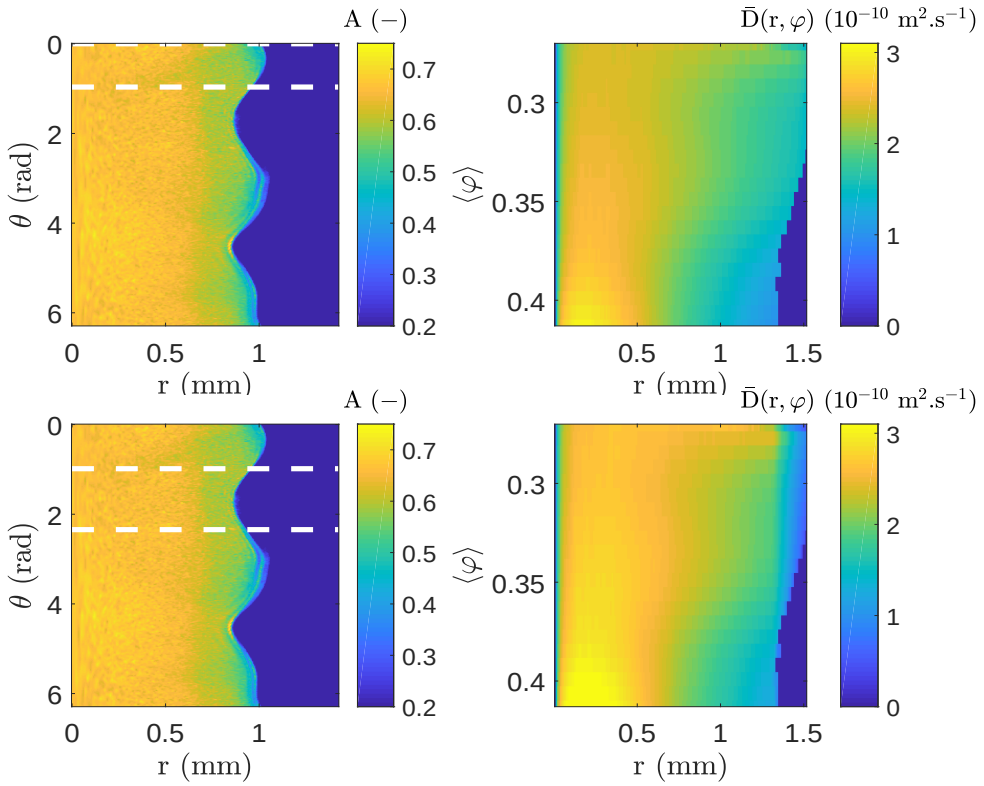

Figure 13: Weighted average D of the time window with respect to the mean concentration and radius position and absorbance in polar coordinates, with an angle interval on which the averaging is done (white dashed lines). The result is shown for two cases: (Top) Interval corresponding to a "hill" (Bottom) Interval corresponding to a "valley".

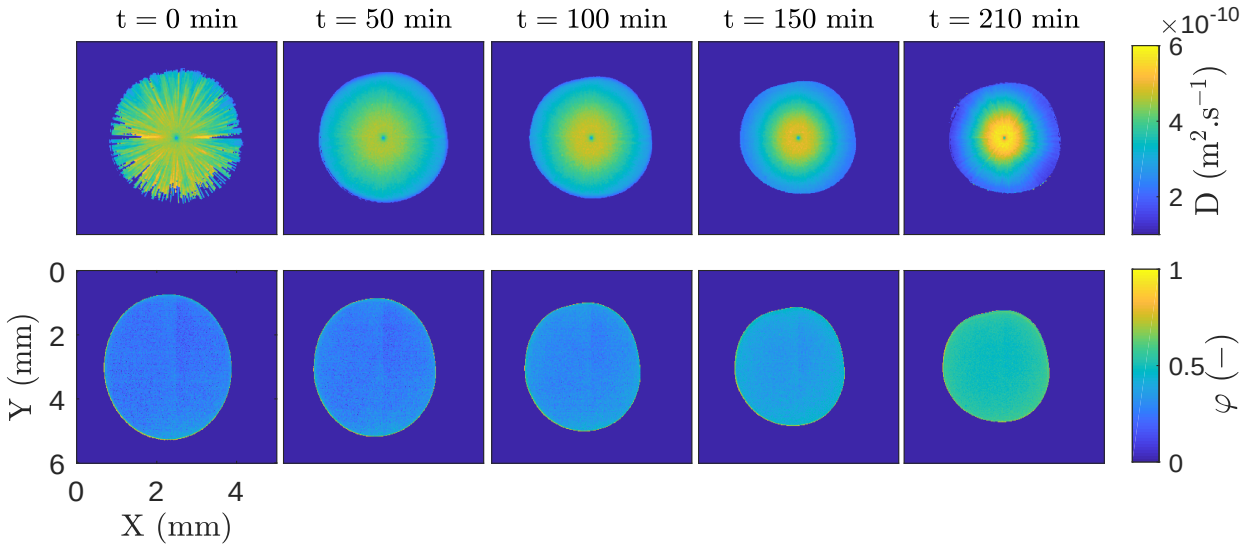

Figure 14: (Top) Mapping of the collective diffusion coefficient of the silica/water mixture as function of time. (Bottom) Mapping of the volume fraction in silica as function of time.

5. Conclusion

In the present work, we took advantage of an IR thermospectroscopy imaging technique to monitor concentration and collective diffusion coefficient fields in a sample evolving in time, with a good spatial resolution. This technique was applied to a bench-marked drying process (the drying in confined geometry) where diffusive mass transfers occur in a fairly predictable manner and these transfers are indeed made clearly visible with the imaging technique we used here. The drying kinetics we monitored is in agreement with the analytical model built in [9], and the measurement of the collective diffusion coefficient of a silica dispersion is in agreement with results presented in [6] using Raman spectroscopy. The strength of the present technique is to offer to possibility to monitor shape and content of a drying material *simultaneously*, along with thermal images even though it is not very beneficial in the present case. We also presented an inverse statistical method directly based on the images and which leads to the intrinsic properties of the material under study. We retrieved the collective diffusion coefficient of the silica dispersion *everywhere* inside the sample. The ability of the technique to generate vast amount of data (spatial coordinates, time and wavelength) makes it particularly interesting for statistical methods. We expect that this technique combined with a robust inverse method could provide fruitful insights on more complicated transient systems, such as for example the drying of chemical hydrogels undergoing drying [19].

In addition, the technique can also provide temperature images of the sample with a good accuracy and spatial resolution. The silica/water mixture exhibited no temperature gradients during drying, and it would therefore be interesting to realize an analogous thermal study of another mixture evolving in time, for example, one with a high phase-change enthalpy. A complete mass balance of water during the drying process could unveil different mechanisms (diffusion, vapourization, convection, etc.).

The main actual limitation concerns the requirement to fix the thickness of the sample in order to get an accurate estimation of temperature and concentration fields. The measurements are confined to the focal plane of the IR camera and provide information only at this position. To unlock this limitation, we are currently extending the versatility of the thermospectroscopy setup by developping an IR tomography technique. Such a 3D imaging technique should allow the construction of both concentration and temperature tomographs of transient systems and therefore reveal potential heterogeneities occurring along the thickness of a material under drying.

Acknowledgements

We thank C. Loussert, A. Bouchaudy for useful discussions and comments, and J.-B. Salmon for a critical reading of the manuscript. We also thank Solvay and *Région Nouvelle-Aquitaine* for funding.

References

[1] G. D. Ewen Smith, *Modern Raman spectroscopy: A practical approach*. Wiley, 2005.

[2] F. Lewiner, J. Klein, F. Puel, and G. Févotte, "On-line ATR FTIR measurement of supersaturation during solution crystallization processes. Calibration and applications on three solute/solvent systems," *Chemical Engineering Science*, vol. 56, pp. 2069–2084, Mar. 2001.

[3] M. Romano, M. Ryu, J. Morikawa, J. Batsale, and C. Pradere, "Simultaneous microscopic measurements of thermal and spectroscopic fields of a phase change material," *Infrared Physics & Technology*, vol. 76, pp. 65–71, May 2016.

[4] L. Daubersies and J.-B. Salmon, "Evaporation of solutions and colloidal dispersions in confined droplets," *Physical Review E*, vol. 84, Sept. 2011.

[5] J. Leng, "Drying of a colloidal suspension in confined geometry," *Physical Review E*, vol. 82, Aug. 2010.

[6] C. Loussert, A. Bouchaudy, and J.-B. Salmon, "Drying dynamics of a charged colloidal dispersion in a confined drop," *Physical Review Fluids*, vol. 1, Dec. 2016.

[7] S. Kirchner, S. Narinsamy, A. Sommier, M. Romano, M. Ryu, J. Morikawa, J. Leng, J. C. Batsale, and C. Pradere, "Calibration procedure for attenuation coefficient measurements in highly opaque media with infrared focal plane array (IRFPA) spectroscopy," p. 31.

[8] F. Boulogne, F. Giorgiutti-Dauphiné, and L. Pauchard, "The buckling and invagination process during consolidation of colloidal droplets," *Soft Matter*, vol. 9, no. 3, pp. 750–757, 2013.

[9] L. Daubersies, J. Leng, and J.-B. Salmon, "Confined drying of a complex fluid drop: phase diagram, activity, and mutual diffusion coefficient," *Soft Matter*, vol. 8, no. 21, p. 5923, 2012.

[10] F. Clément and J. Leng, "Evaporation of liquids and solutions in confined geometry," *Langmuir*, vol. 20, no. 16, 2004.

[11] E. N. L. R. Byron Bird, Warren E. Stewart, *Transport phenomena*. J. Wiley, 2nd, wiley international ed ed., 2002.

[12] A. Bouchaudy and J.-B. Salmon, "Drying-induced stresses before solidification in colloidal dispersions: in situ measurements," *Soft Matter*, vol. 15, pp. 2768–2781, 2019.

[13] B. Selva, L. Daubersies, and J.-B. Salmon, "Solutal Convection in Confined Geometries: Enhancement of Colloidal Transport," *Physical Review Letters*, vol. 108, May 2012.

[14] J.-B. Salmon and F. Doumenc, "Buoyancy-driven dispersion in confined drying of liquid binary mixtures," *arXiv:2001.04662 [cond-mat]*, Jan. 2020. arXiv: 2001.04662.

[15] C. Pradere, C. Hany, J. Toutain, and J.-C. Batsale, "Thermal Analysis for Velocity, Kinetics, and Enthalpy Reaction Measurements in Microfluidic Devices," *Experimental Heat Transfer*, vol. 23, pp. 44–62, Dec. 2009.

[16] C. Hany, C. Pradere, J. Toutain, and J.-C. Batsale, "A millifluidic calorimeter with infrared thermography for the measurement of chemical reaction enthalpy and kinetics," *Quantitative InfraRed Thermography Journal*, vol. 5, pp. 211–229, Dec. 2008.

[17] M. Bamford, J. C. Batsale, and O. Fudym, "Nodal and modal strategies for longitudinal thermal diffusivity profile estimation: Application to the non destructive evaluation of SiC/SiC composites under uniaxial tensile tests," *Infrared Physics & Technology*, vol. 52, pp. 1–13, Jan. 2009.

[18] C. Ravey, C. Pradere, N. Regnier, and J.-C. Batsale, "New temperature field processing from IR camera for velocity, thermal diffusivity and calorimetric non-intrusive measurements in microfluidics systems," *Quantitative InfraRed Thermography Journal*, vol. 9, pp. 79–98, June 2012.

[19] A. Turani-i Belloto, N. Meunier, P. Lopez, and J. Leng, "Diffusion-limited dissolution of calcium carbonate in a hydrogel," *Soft Matter*, vol. 15, pp. 2942–2949, 2019.